RSC Advances

PAPER

View Article Online
View Journal | View Issue

Check for updates

Cite this: *RSC Adv.*, 2026, **16**, 14361

Synergistic ultrafine steel slag and fly ash for steel passivation in sustainable ternary cements: Temperature-dependent stability and composition regulation

Ying Lin,[ab] Zhiwei Wu,[ab] Zhengxian Yang *[ab] and Hesong Jin*[c]

The utilization of industrial by-products like ultrafine steel slag (USS) and fly ash (FA) in cementitious systems offers a pivotal strategy for decarbonizing the construction sector and valorizing solid waste. This study investigates the synergistic role of USS and FA in designing and regulating the passive film on reinforcing steel within sustainable ternary cements, with a particular focus on its temperature-dependent stability. Through an integrated approach of pore solution chemistry, multi-scale electrochemistry, and surface characterization, we deciphered the coupled mechanisms of ion transport, passive film evolution, and defect chemistry governed by the composition. The results indicate that while FA elevates K^+ concentration, it reduces pore solution alkalinity (pH 12.56), falling below the passivation threshold. A moderate USS content (30%) optimally compensates by dissolving Ca-bearing phases, restoring the pH to levels conducive to passivation (12.95), and facilitating the formation of a superior bilayer passive film. This regulated film exhibits high impedance, low defect density, and an inner barrier layer enriched with Fe^{2+} and lattice oxygen, offering exceptional protection. Conversely, excessive USS incorporation (50%) increases surface roughness by 63%, exacerbating heterogeneity and ionic permeability, Furthermore, the stability of this optimal formulation demonstrates a critical temperature dependence. Curing at ≥40 °C accelerates film hydration and hydroxylation. It also promotes deep-layer defect proliferation, which markedly degrades the protective performance. This work unveils the fundamental mechanisms of composition-driven passivation, providing a principle for designing sustainable low-carbon cementitious systems by tailoring properties to achieve long-term material service life.

Received 16th December 2025
Accepted 9th March 2026

DOI: 10.1039/d5ra09738j

rsc.li/rsc-advances

Open Access Article. Published on 16 March 2026. Downloaded on 5/1/2026 12:22:37 AM.
This article is licensed under a Creative Commons Attribution-NonCommercial 3.0 Unported Licence.

1. Introduction

The utilization of industrial by-products such as steel slag (SS) and fly ash (FA) in cementitious systems represents a strategic pathway toward reducing the carbon footprint of concrete and promoting circular economy principles in construction. SS, which contains hydraulic phases like C_2S and C_3S, has shown potential as a supplementary cementitious material.[1–3] However, its practical application is often hindered by dense crystallinity, coarse particle size, and the presence of RO phases with minor free CaO and MgO, which retard hydration and pose risks to volume stability at high replacement levels.[4,5] Mechanical activation *via* ultrafine grinding offers a promising route to mitigate these limitations. Previous studies have demonstrated that finely ground SS can replace up to 60% of cement, with early hydration of free lime and periclase mitigating long-term expansion.[6,7] Nevertheless, the influence of ultrafine steel slag (USS) on the passivation behaviour and stability of the passive film on reinforcing steel remains poorly understood.

FA, another widely used supplementary cementitious material, contributes to sustainable concrete production by lowering CO_2 emissions, conserving raw materials, and enhancing long-term performance.[8] Through pozzolanic, filler, and fineness effects, FA refines the pore structure and delays depassivation of steel reinforcement. However, its low early reactivity can impair initial corrosion resistance.[9,10] USS, with its capacity to rapidly release Ca^{2+} and OH^- ions, may compensate for the slow early kinetics of FA, though its standalone use is constrained by volumetric and reactivity concerns.[11,12] Recent evidence suggests that blending USS with FA yields synergistic benefits: USS-derived alkalis can activate FA's pozzolanic reaction, suppress expansive phases, and optimize pore solution chemistry, thereby enhancing the protective quality of the passive film.[13] Despite these advances, the microstructural evolution of

[a]*State Key Laboratory of Green and Efficient Development of Phosphorus Resources, College of Civil Engineering, Fuzhou University, Fuzhou 350108, China. E-mail: zxyang@fzu.edu.cn*

[b]*Joint International Research Laboratory of Deterioration and Control of Costal and Marine Infrastructures and Materials, College of Civil Engineering, Fuzhou University, Fuzhou 350108, China*

[c]*Department of Infrastructure Engineering, The University of Melbourne, Parkville, VIC 3010, Australia. E-mail: jhs199315@my.swjtu.edu.cn*

© 2026 The Author(s). Published by the Royal Society of Chemistry

Open Access Article. Published on 16 March 2026. Downloaded on 5/1/2026 12:22:37 AM. This article is licensed under a Creative Commons Attribution-NonCommercial 3.0 Unported Licence.

the passive film in USS-FA ternary systems in terms of Fe^{3+}/Fe^{2+} distribution, defect density, and FeOOH crystallinity has not been systematically elucidated.

In highly alkaline environments such as simulated pore solutions (SPS), reinforcing steel undergoes spontaneous passivation, forming a multi-layered oxide film through coupled electrochemical and precipitation processes.[14,15] This film typically exhibits a bilayer structure: a dense, Fe^{2+}-rich inner barrier (*e.g.*, FeO or Fe_3O_4) and a more porous, Fe^{3+}-rich outer layer composed of oxyhydroxides such as γ-Fe_2O_3 and α-FeOOH.[16,17] The formation sequence follows the oxidation pathway $Fe^0 \rightarrow Fe^{2+} \rightarrow Fe^{3+}$, with gradients in composition, defect density, and crystallinity evolving with depth.[18–20] The stability of this passive layer is governed by lattice defects, cation incorporation, and anion vacancies,[21–23] while its transformation among magnetite, maghemite, and goethite is modulated by electrochemical potential, pH, and ionic composition.[24,25] Pore solution chemistry, including the balance of cations and anions, ionic strength, and alkalinity, plays a decisive role in the stability and protectiveness of passive films.[26,27] In ordinary Portland cement (OPC) systems, high concentrations of Na^+, K^+, Ca^{2+}, and OH^- sustain pH values above 12.5, facilitating rapid passivation.[28,29] The incorporation of FA, however, reduces [Ca^{2+}] and [OH^-] through the consumption of portlandite, thereby lowering both pH and ionic strength, despite partial compensation by released alkalis.[30–32] Similarly, SS releases Ca^{2+} and OH^- more slowly than OPC, further depressing early-age pH and ionic strength.[33,34] In SS–FA blends, early Ca^{2+} and alkalinity provided by SS can activate FA, while FA-derived aluminosilicates sequester Ca^{2+}, collectively modulating phase equilibria and ionic transport.[35,36] The resulting high-pH environment promotes the formation of a bilayer passive film, with compact inner and porous outer regions.[37] Alkali cations facilitate uniform oxide growth,[38,39] whereas Ca^{2+} incorporation may induce lattice distortion and favor $Ca(OH)_2$ precipitation, increasing defect density and compromising film continuity.[40,41] Anions such as SO_4^{2-} can adsorb at active sites and influence the precipitation kinetics of iron oxides and oxyhydroxides.[42,43] Thus, the interplay among cation and anion adsorption, pH, and redox conditions governs the Fe^{3+}/Fe^{2+} ratio, oxide crystallinity,[44,45] and the overall stability and repairability of the passive film.[46,47]

Temperature is another critical factor influencing steel passivation and corrosion in concrete, affecting ion mobility, oxide transformation kinetics, and dissolution-precipitation equilibria.[48,49] Elevated temperatures generally accelerate ionic transport and phase transitions, leading to thinner films, higher defect densities, and reduced corrosion resistance.[50–52] In saturated $Ca(OH)_2$ solutions, higher temperatures delay initial passivation, enhance film dissolution, and lower pitting potentials, increasing susceptibility to localized attack. Temperature also affects dissolved oxygen content, which influences cathodic kinetics and anodic dissolution rates.[53,54] Under field conditions, solar radiation and climatic extremes can raise steel temperatures by 30–50 °C above ambient, and in severe cases, up to 90 °C.[55] Such thermal fluctuations introduce repeated cycling, inducing interfacial shear stresses, microcracking, and defect generation in the passive film, thereby undermining its protective function.[56]

Given that USS and FA significantly alter pore solution chemistry, the passivation behavior in USS–FA–OPC ternary systems is expected to differ markedly from that in plain OPC. To address this gap, this study systematically investigates the coupled effects of binder composition and temperature on passive film formation and stability. The temporal evolution (2 h to 14 days) of ionic concentration, pH, and ionic strength across a range of USS/FA blends was quantified and correlated with electrochemical metrics, including open-circuit potential (OCP), electrochemical impedance spectroscopy (EIS), and Mott–Schottky (M–S) analysis, to track film growth and semiconducting behavior. For the optimal mix, the influence of temperature (20–50 °C) on charge-transfer resistance and film structure was further evaluated using EIS, M–S, and X-ray photoelectron spectroscopy (XPS). Depth-profiling XPS, scanning electron microscopy (SEM), and atomic force microscopy (AFM) are employed to resolve compositional gradients, morphology, and roughness of the passive films. Different from similar reports on ternary binders that mainly emphasize hydration or bulk durability, and corrosion studies that often discuss pore solution alkalinity qualitatively, this work explicitly links USS-induced ionic redistribution to passive-film electronic defect descriptors (N_{D1}/N_{D2} and *C–V*/EIS signatures), enabling identification of a practical USS replacement window (20–30%) for robust passivation. This provides actionable mix-design implications for real reinforced concrete by indicating how to sustain passivation and delay depassivation under chloride ingress or carbonation exposure. The outcomes of this work are expected to establish a chemistry–structure–property framework for passive films under multi-factor interactions, supporting the durable and low-carbon design of reinforced concrete in aggressive environments.

2. Experimental program

2.1. Raw materials

The ordinary low-carbon steel bars used in this study were supplied by Shengxin Technology Co., Ltd, China and conformed to the HRB400 designation. The chemical composition of the ribbed HRB400 steel (wt%) was: C, 0.23; Si, 0.54; Mn, 1.42; P, 0.03; S, 0.02; with the balance Fe. The SS, FA, and OPC were provided by Yuanxin Building Materials Co., Ltd, China. The USS had a specific surface area of 760 $m^2\ kg^{-1}$. This material was produced from ordinary steel slag through a multi-step size reduction and activation process. This process involved primary processing *via* rod milling for iron removal and screening, followed by secondary grinding in a planetary ball mill for 4 h. The intensive comminution not only reduced the particle size to the ultrafine range but also created fresh, highly reactive surfaces, thereby improving its dissolution kinetics and overall cementitious performance. The chemical compositions of the raw materials used in this study are listed in Table 1.

© 2026 The Author(s). Published by the Royal Society of Chemistry

Open Access Article. Published on 16 March 2026. Downloaded on 5/1/2026 12:22:37 AM. This article is licensed under a Creative Commons Attribution-NonCommercial 3.0 Unported Licence.

Table 1 Chemical composition of USS, FA and OPC (wt%)

	CaO	SiO_2	Al_2O_3	Fe_2O_3	MgO	Na_2O	K_2O	SO_3
USS	42.66	24.93	8.3	16.72	6.08	0.57	0.38	0.36
FA	23.25	31.07	36.24	2.88	4.3	0.44	0.76	2.11
OPC	62.24	21.80	5.12	3.91	3.15	0.31	0.47	3.00

Table 2 Mix proportion of SPS (g)

Group	USS	FA	OPC
OPC	0	0	100
US5FA0C	50	00	50
US4FA1C	40	10	50
US3FA2C	30	20	50
US0FA5C	0	50	50

2.2. Mix proportion and sample preparation

To address the limited availability of pore solution in hardened concrete and the low yield of high-pressure extraction (1 mL per 250 g sample), this study adopted a modified SPS preparation protocol.[57] The SPS was prepared by homogenizing dry binders (Table 2) with deionized water (water/binder = 1.0) *via* rotary mixing for 24 h. The slurry was vacuum-filtered sequentially through qualitative filter paper followed by 0.2 μm membrane. Filtrates were stored at 4 ± 2 °C and noted as US–FA–C SPS.

The reinforcing steel specimens were mounted in cylindrical rubber molds, ground with SiC papers (250–2000 grit), and polished to a mirror finish using 0.5 μm diamond suspension on a UNIPOL-1000D polisher. Surface preparation for SEM/AFM/XPS involved gradient ultrasonic cleaning and argon encapsulation. For electrochemical tests, samples were mounted in PTFE holders with a fixed exposed area of 1.00 cm^2, with immersion durations determined by experimental design.

2.3. Test methods

2.3.1. Chemical composition and concentration analysis of SPS. The alkalinity of US–F–C SPS was measured using a PHS-3E pH meter (INESA, Shanghai) at 23 ± 2 °C on 20 mL aliquots, with triplicate readings averaged. Ionic composition was determined by ICP-OES (Thermo iCAP 6300) for major cations (Na^+, K^+, Ca^{2+}, Mg^{2+}, Al^{3+}), while OH^- concentration was *via* ion chromatography (Metrohm 883 Basic IC plus).

2.3.2. Electrochemical tests. Electrochemical tests were performed using an Autolab VIONIC workstation (Metrohm) in a three-electrode cell, with reinforcing steel (1.00 cm^2) as the working electrode, Pt foil (2.0 × 2.0 cm) as the counter, and a saturated calomel electrode (SCE) as reference. Temperature measurements were conducted isothermally at 20 °C and under controlled temperatures (30 °C, 40 °C, and 50 °C) using a 13 L thermostatic bath (±0.5 °C). The OCP defined as the steady-state potential difference between working and reference electrodes, reflects the passivation status of steel. An OCP plateau with fluctuations less than ±20 mV indicates formation of a stable passive film. In this study, OCP was recorded at 10 Hz over 60 s using VIONIC workstation. EIS was employed to monitor passive film evolution on steel during 14 days immersion in SPS. A sinusoidal voltage perturbation with a 10 mV amplitude applied across 0.01 Hz to 100 kHz; triplicate spectra (deviation <5%) were fitted using a Randles circuit in ZSimpWin to extract resistance and capacitance parameters, which quantify film compactness and corrosion protection kinetics. M–S analysis was conducted to investigate the semiconductor properties of the passive film by characterizing the capacitance-potential response of the space-charge region at the film/solution interface. A high-frequency AC signal at 1 kHz with an amplitude of 10 mV was superimposed on a linear potential sweep ranging from −0.5 V to 0.5 V *versus* SCE.

2.3.3. Chemical composition and morphology of passivation film. The XPS (PHI 5000 VersaProbe III) was employed to analyze passive film chemistry under ultra-high vacuum (<6.7 × 10^{-8} Pa) using a monochromatic Al Kα source (1486.6 eV, 20 kV, 15 mA). The instrument offered <3 μm spatial resolution and 0.1 at% detection limits. All spectra were charge-corrected to the adventitious C 1s peak at 284.8 eV, and peak fitting/quantification was performed with MultiPak software to determine elemental compositions and chemical states. The SEM (Quanta 250, FEI) was used to examine passive film morphology in US–FA–C systems under solution conditions. High-vacuum imaging was performed at accelerating voltages of 0.2–30 kV (beam current ≤ 2 μA), with resolutions of 3.0 nm at 30 kV and 8.0 nm at 3 kV. Elemental composition was further analyzed by energy-dispersive X-ray spectroscopy (EDS, 129 eV resolution). The AFM (Agilent 5500 series) in contact mode was used to characterize the 3D morphology and roughness of passive films in different US–FA–C systems. Scans were conducted over 9 μm × 9 μm areas with system noise levels of XY < 1 Å RMS and Z < 0.2 Å RMS, enabling high-resolution mapping of nanoscale topography.

3. Results and discussion

3.1. Chemical composition and concentration analysis of the SPS

3.1.1. Chemical composition and ionic concentration of SPS. The ion concentration profile (Fig. 1) reveals K^+ dominance across all mixtures, though its origin and evolution vary with composition. In the OPC system, lower K^+ concentrations

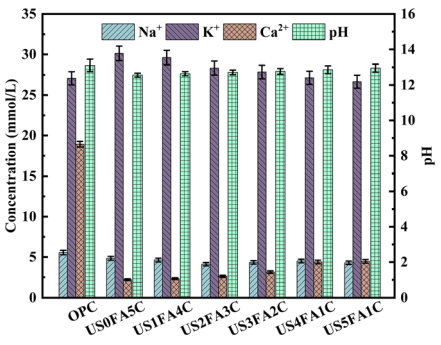

Fig. 1 Cation concentration of SPS.

Open Access Article. Published on 16 March 2026. Downloaded on 5/1/2026 12:22:37 AM. This article is licensed under a Creative Commons Attribution-NonCommercial 3.0 Unported Licence.

indicate limited potassium release from cement. Conversely, US0FA5C (50% FA substitution) exhibits significantly elevated K^+ levels, confirming FA's potassium-rich phases as the primary source. Notably, despite 50% cement reduction, FA incorporation not only compensates but increases net K^+ concentration. Progressive USS substitution for FA reduces K^+ concentration linearly, demonstrating USS's dilution effect due to its negligible soluble potassium content.

Meanwhile, with increasing USS dosage from US0FA5C to US5FA0C, the overall ionic distribution shifts noticeably. Ca^{2+} concentration exhibits a gradual increase, rising from approximately 2 mmol L^{-1} in US0FA5C to around 4 mmol L^{-1} in US5FA0C. This increase is mainly attributed to the greater Ca-bearing inventory of USS and its faster dissolution-hydration kinetics. CaO (including free CaO) and Ca-rich silicates (*e.g.*, C_2S and C_3S) in USS hydrate/dissolve under alkaline conditions, continuously supplying Ca^{2+} together with OH^-. The ultrafine nature of USS (specific surface area $\approx$760 m^2 kg^{-1}) further accelerates ion release by providing a larger reactive surface and more active sites. In addition, substituting FA decreases the aluminosilicate fraction capable of immobilizing Ca^{2+} *via* early hydrate formation, which also contributes to the higher residual Ca^{2+} level in solution. In contrast, Na^+ concentrations remain relatively stable across all mixtures, implying a more uniform release behavior that is less sensitive to binder composition changes. A moderate correspondence is observed between the trends in ionic concentration and pH (Fig. 1) evolution as the proportion of USS increases from 0% to 50% in the US–FA–C ternary pore solution system, replacing FA at a fixed cement dosage. In USS-free systems (US0FA5C), the solution exhibits the lowest pH (approximately 12.56) and Ca^{2+} concentration, attributed to limited calcium release from FA and reduced $Ca(OH)_2$ formation. As USS content increases, Ca^{2+} concentrations rise gradually from approximately 2 mmol L^{-1} to approximately 4.5 mmol L^{-1}, accompanied by a systematic increase in pH up to approximately 12.95 in US5FA0C. This trend suggests that USS contributes reactive calcium and magnesium oxides, which progressively dissolve to release OH^-, enhancing the solution's alkalinity without increasing cement content. K^+ levels remain stable across all blends due to the fixed cement proportion, while Na^+ concentrations are consistently low, reflecting minimal sodium contribution from both USS and FA. Although nonlinear, the coordinated rise in Ca^{2+} and pH underscores USS's role in compensating for alkalinity loss from FA substitution and promoting a favorable chemical environment for passive film formation on reinforcing steel.

3.1.2. Ionic strength and oxygen solubility of SPS. The ionic strength (I_i) of the SPS varies systematically with the replacement of FA by USS at a fixed OPC fraction (50 wt%). The OPC reference sample exhibits the highest I_i (196.1 mmol kg^{-1}), consistent with its elevated concentrations of soluble Ca^{2+}, K^+, and associated hydroxides released during hydration. Partial substitution of OPC by FA–USS blends reduces I_i sharply to values between 110–145 mmol kg^{-1}. The lowest I_i values occur in FA-rich, low-USS mixtures (US0FA5C: 109.9 mmol kg; US1FA4C: 111.5 mmol kg; US2FA3C: 110.5 mmol kg^{-1}), indicating significant dilution of multivalent metal cations and alkali ions. When USS content exceeds approximately 30 wt% (US3FA2C: 123.6 mmol kg; US4FA1C: 134.9 mmol kg; US5FA0C: 144.8 mmol kg^{-1}), I_i increases progressively. This trend aligns with the gradual dissolution of basic oxides (*e.g.*, CaO, MgO, Fe-bearing phases) from USS, which replenishes the pore solution with ionic concentration.

Dissolved oxygen (O_2) in electrolyte solutions exhibits an inverse correlation with I_i due to salting-out behavior; elevated I_i suppresses O_2 solubility. Consequently, FA-rich systems with low I_i maximize O_2 availability, whereas OPC pore solutions minimize it. USS-rich mixtures occupy an intermediate position, despite higher I_i than FA systems, their I_i remains substantially below OPC levels, enhancing O_2 accessibility relative to cementitious environments. FA-dominated mixes improve O_2 transport but slow passivation due to lower alkalinity (pH 12.2–12.8). USS-rich systems enhance passive film formation with high alkalinity (pH > 13.2), even with less dissolved O_2. The hybrid US3FA2C offers a balance: moderate I_i, ideal alkalinity (pH 13.0 $\pm$ 0.1), and stability comparable to OPC. Overall, steel passivation is controlled by two competing factors. USS increases alkalinity and promotes film formation, whereas higher ionic strength suppresses dissolved O_2 and can slow the cathodic process.

3.2. Electrochemical properties of passivation film

3.2.1. Passivation potential of passive film. Fig. 2 shows the OCP evolution of steel reinforcement in SPS derived from distinct binder systems. All compositions exhibit rapid OCP increase within 24 h–48 h followed by stabilization, aligning with the two-stage passivation mechanism. OCP > −250 mV signifies passivity, while −400 mV to −250 mV indicates active corrosion. In USS-containing systems, OCP rose to −281 mV at 24 h, exceeded −250 mV by 48 h, and stabilized near −150 mV post-immersion, demonstrating progressive formation of a stable passive layer. Among USS-bearing mixtures, the US3FA2C exhibited OCP evolution closely resembling that of the OPC control, indicating comparable passivation kinetics and film stability. In contrast, mixtures with lower USS content (US0FA5C and US1FA4C) showed slower OCP increases and more negative steady-state potentials (approximately −140 to

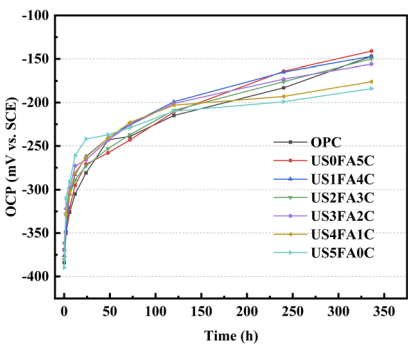

Fig. 2 OCP characterization of SPS.

© 2026 The Author(s). Published by the Royal Society of Chemistry

Open Access Article. Published on 16 March 2026. Downloaded on 5/1/2026 12:22:37 AM.
This article is licensed under a Creative Commons Attribution-NonCommercial 3.0 Unported Licence.

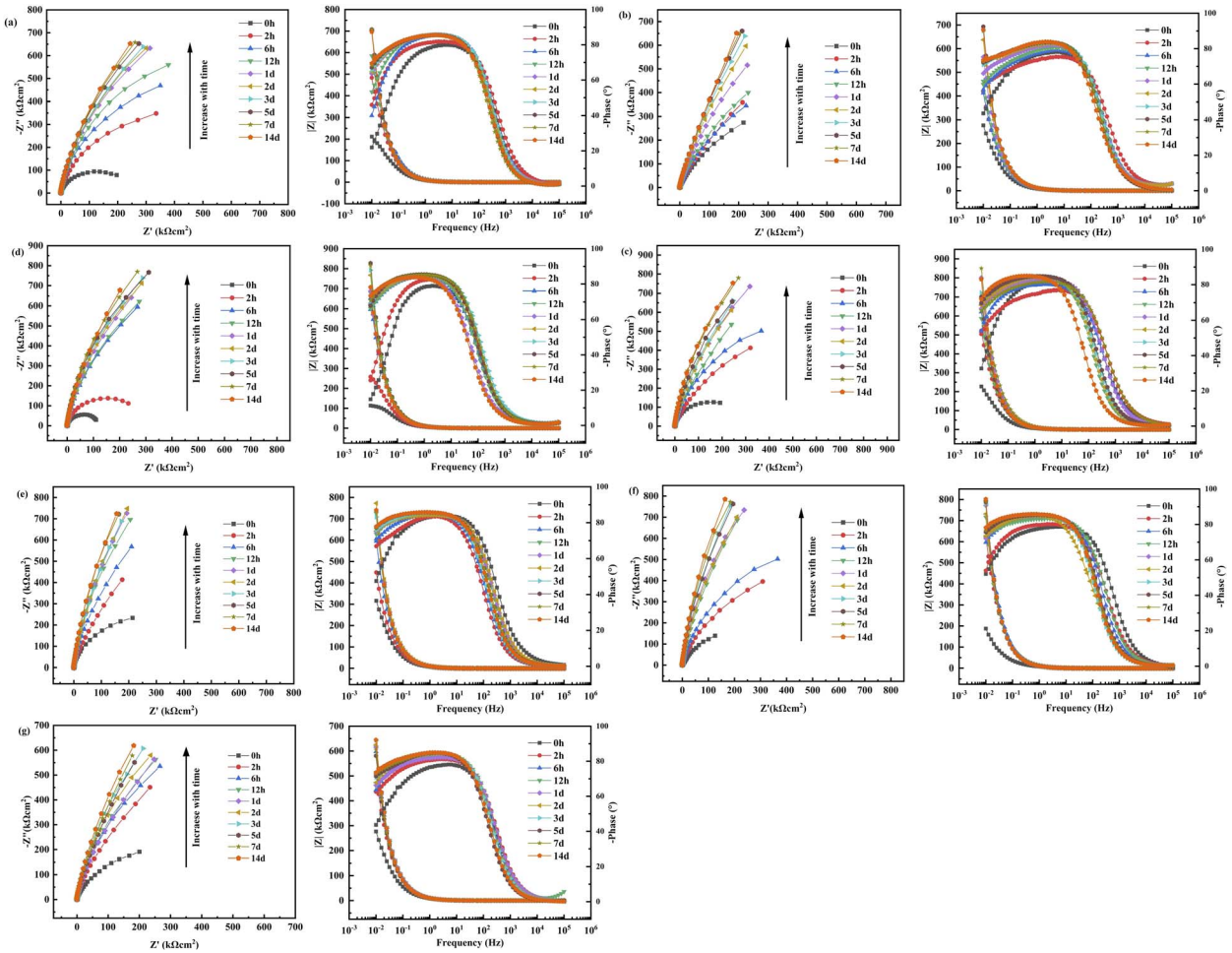

Fig. 3 Nyquist plots and Bode plats of (a) OPC, (b) US0FA4C, (c) US1FA4C, (d) US2FA3C, (e) US3FA2C, (f) US4FA1C, and (g) US5FA0C.

−145 mV), attributed to reduced alkalinity and limited ionic availability hindering early-stage passivation. Conversely, the high-USS system (US5FA0C) promoted rapid initial OCP rise due to elevated OH^-, yet its final OCP remained lower (approximately −180 mV), suggesting long-term instability or passive film heterogeneity. These results demonstrate that near 30% USS achieves an optimal balance between alkalinity, ion release, and protective film formation, yielding passivation behavior similar to OPC. Excessive USS (>30%) may alter electrochemical conditions and compromise long-term corrosion resistance.

3.2.2. Electrochemical impedance characterization of passive film. Fig. 3a–g presents the Nyquist and Bode plots characterizing the time-dependent electrochemical behavior of reinforcing steel in systems incorporating various USS dosages. In the OPC system (Fig. 3a), the radius of the impedance arc exhibits a continuous increase with immersion time, and the initially low impedance gradually increases and stabilizes at a higher level by 14 days, indicating the progressive formation of a compact and protective passive film. In contrast, the US0FA5C system (Fig. 3b), with high FA content and absence of USS, shows the slowest impedance growth and the lowest final impedance, suggesting that excessive FA hinders the nucleation and development of the passive film in the early stages.

As the USS content increases from US1FA4C to US3FA2C (Fig. 3c–e), both the semicircle diameter in the Nyquist plots and the mid-frequency phase angle plateau in the Bode spectra increase significantly. The US3FA2C system exhibits the highest impedance values and the broadest phase angle plateau throughout the immersion period, indicating the formation of a highly uniform and electronically stable passive film. It is noted that US4FA1C and US5FA0C systems (Fig. 3f and g) maintain high impedance at later stages. However, the early-stage passivation (within 6 h) is relatively delayed, especially for US5FA0C, where minimal impedance increase is observed. This delayed response implies that excessive USS may suppress the availability or transport of reactive ionic species in the solution, thereby slowing the passivation kinetics. These results indicate that a moderate USS content, such as in the US3FA2C mix, not only facilitates rapid passive film formation but also enhances its structural integrity, while excessive USS incorporation may adversely affect early film growth. The evolution of the impedance spectra, reflected by expanded capacitive arcs and elevated low-frequency impedance with broadened phase

Open Access Article. Published on 16 March 2026. Downloaded on 5/1/2026 12:22:37 AM. This article is licensed under a Creative Commons Attribution-NonCommercial 3.0 Unported Licence.

Table 3 EIS fitting results of steel bars after passivation in SPS for 2 h

Specimen	R_s (Ω cm^2)	R_p (kΩ cm^2)	Q		Chi-square ($\chi^2/\times10^{-4}$)
			Y_0 (10^{-5} Ω^{-1} cm^{-2} s^n)	n	
OPC	34.26	74.7	1.74	0.91	5.3
US0FA5C	62.59	105.3	1.81	0.83	3.61
US1FA4C	68.48	278.0	1.48	0.93	3.73
US2FA3C	59.54	342.3	1.43	0.92	1.64
US3FA2C	56.63	443.6	1.30	0.94	5.66
US4FA1C	57.46	248.5	1.27	0.89	9.62
US5FA0C	52.64	125.0	1.89	0.90	10.4

angle plateaus, confirms the improvement in both dielectric properties and corrosion resistance of the passive layer.

The EIS behavior of passive films can be adequately described using the simplest equivalent circuit, consisting of a resistor and a capacitor in parallel. Consequently, the overall interfacial characteristics of passivated metals can be represented by a modified Randles circuit, expressed as R(QR). In this model, R_s denotes the solution resistance, R_p represents the resistance of the passive film, and C_p represents a non-ideal constant phase element (CPE), reflecting the capacitive-like response of the entire interface.

The fitted parameters obtained from 2 h immersion are summarized in Table 3. At the early stage (2 h), the OPC sample exhibits the lowest R_p (74.7 kΩ cm^2), reflecting an initially weak and porous passive film. The incorporation of FA (US0FA5C) slightly increases R_p to 105.3 kΩ cm^2, yet the accompanying increase in Y_0 and decrease in n value ($Y_0 = 1.81 \times 10^{-5}$ S s^n cm^{-2}, $n = 0.83$) indicate a more heterogeneous and defective interfacial structure. As the USS content increases, a significant enhancement in film resistance is observed, particularly for the US1FA4C and US3FA2C systems, with R_p reaching 278.0 and 342.3 kΩ cm^2, respectively. The latter also displays a relatively low Y_0 and high n ($Y_0 = 1.64 \times 10^{-5}$ S s^n cm^{-2}, $n = 0.94$), suggesting the formation of a compact and homogeneous passive layer.

With continued immersion up to 14 days, the passive film resistance in all specimens exhibits a substantial increase, reflecting the further growth and densification of the oxide layer. As shown in Table 4, the OPC system achieves the highest R_p (2314 kΩ cm^2), confirming the development of a dense and electronically insulating passive film in the Portland cement matrix. In comparison, nevertheless, the US0FA5C system, although lacking USS, maintains a relatively high R_p (2173 kΩ cm^2), indicating that the influence of FA becomes less detrimental over prolonged passivation periods. For USS-containing systems, moderate slag incorporation (20–30% USS; US1FA4C–US3FA2C) results in comparable R_p values ranging from 1600 to 1700 kΩ cm^2, implying that USS dosages up to 30% do not compromise long-term passive film integrity. Among them, the US3FA2C system presents a favorable combination of low admittance ($Y_0 = 1.74 \times 10^{-5}$ S s^n cm^{-2}) and high phase exponent ($n = 0.93$), suggesting a well-developed and compact dielectric film. However, when the USS content is further increased to 40% and above (US4FA1C and US5FA0C), R_p declines markedly (1235 and 1456 kΩ cm^2, respectively), despite minimal variation in CPE characteristics. This reduction likely stems from structural inhomogeneities or insufficient pozzolanic activation at high USS contents, which compromises the film's protective capacity. Taken together, the results suggest that while early-stage passivation benefits from USS incorporation, long-term passivation performance reaches an optimal threshold at moderate slag dosages, beyond which excessive substitution may be counterproductive.

3.2.3. Semiconductor properties of passive film. Fig. 4 shows the M–S (left) and concurrently measured capacitance–voltage (C–V) (right) plots, which reveal the evolution of semiconductor behavior and defect density within the passive films over immersion time for different blended systems. For the OPC system (Fig. 4a), the M–S plot at 2 h exhibits a pronounced positive slope and the highest C^{-2} values, indicating a low donor density and well-defined space charge region. However, prolonged immersion to 14 days leads to slope reduction and curve flattening, suggesting increased defect density and structural degradation, which is corroborated by the rising and unstable capacitance in the corresponding C–V plot. A similar

Table 4 EIS fitting results of steel bars after passivation in SPS for 14 days

Specimen	R_s (Ω cm^2)	R_p (kΩ cm^2)	Q		Chi-square ($\chi^2/\times10^{-4}$)
			Y_{0f} (10^{-5} Ω^{-1} cm^{-2} s^n)	n_f	
OPC	48.53	2314	1.58	0.92	5.40
US0FA5C	87.25	2173	1.60	0.92	2.46
US1FA4C	65.05	1698	1.78	0.93	2.94
US2FA3C	68.37	1635	1.88	0.94	5.29
US3FA2C	105.2	1602	1.74	0.92	1.88
US4FA1C	95.08	1235	2.31	0.93	1.10
US5FA0C	73.59	1456	1.95	0.92	7.93

© 2026 The Author(s). Published by the Royal Society of Chemistry

Open Access Article. Published on 16 March 2026. Downloaded on 5/1/2026 12:22:37 AM.
This article is licensed under a Creative Commons Attribution-NonCommercial 3.0 Unported Licence.

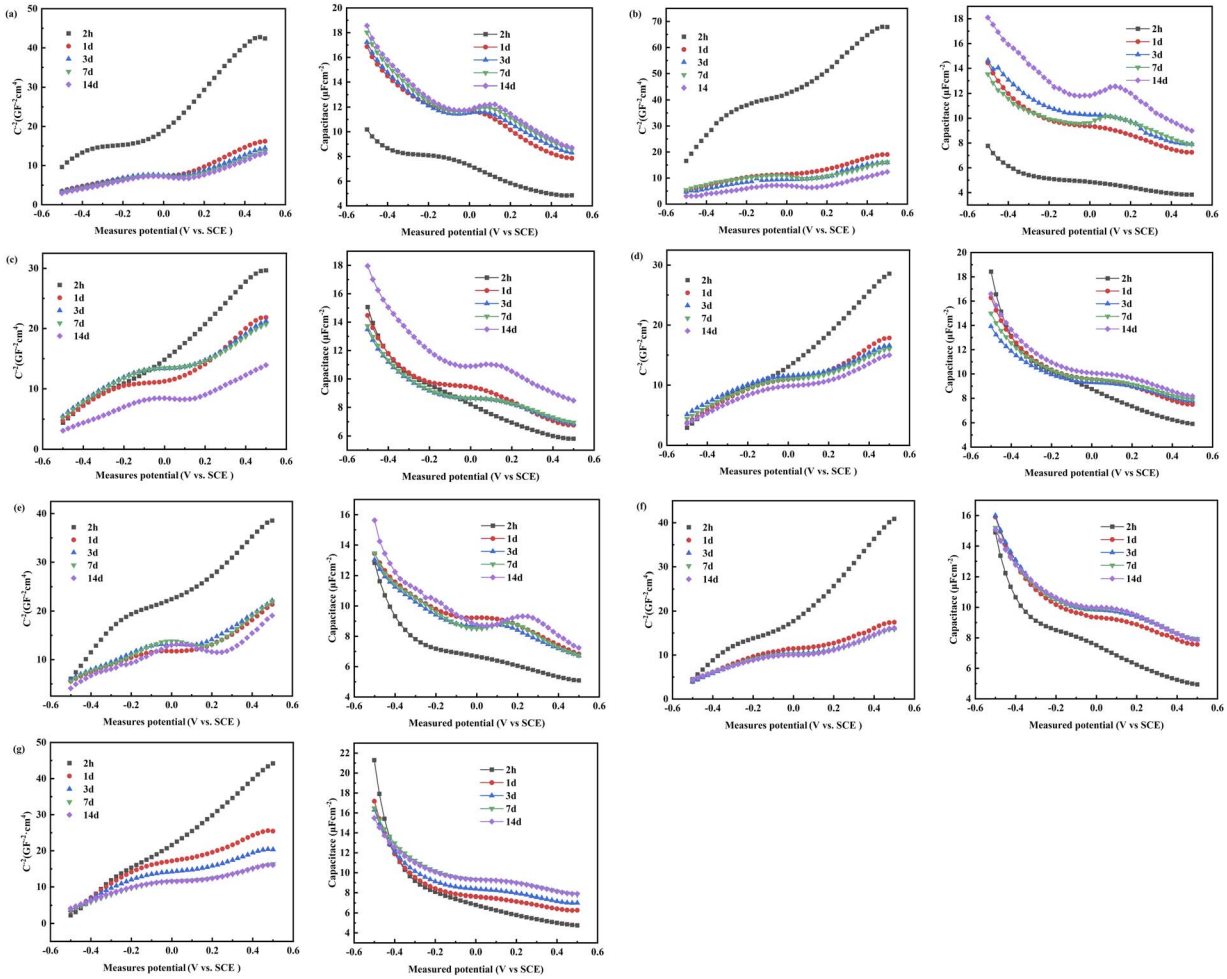

Fig. 4 M–S (left) and *C–V* (right) plots of reinforcing steel in (a) OPC, (b) US0FA5C, (c) US1FA4C, (d) US2FA3C, (e) US3FA2C, (f) US4FA1C, and (g) US5FA0C SPS systems.

deterioration trend is observed in the FA-dominated US0FA5C system (Fig. 4b), where the slope steadily decreases beyond 3 d, reflecting compromised insulating properties due to the low reactivity of FA.

In contrast, the introduction of USS significantly improves the semiconducting properties of the passive film. In the US1FA4C system (Fig. 4c), M–S curves from 1 to 7 days show consistently steeper slopes than at 14 days, indicating a progressive decrease in donor density and improved film compactness. This trend is further enhanced in US2FA3C and US3FA2C systems (Fig. 4d and e), where the films display near-linear M–S behavior with relatively steep slopes between −0.3 V and 0.2 V, particularly at 3–7 days, suggesting a uniform n-type semiconducting character with low defect concentration. The corresponding *C–V* curves for these systems show minimal humps and stable overlapping profiles, confirming the formation of a homogeneous and electronically robust passive layer. The US3FA2C sample, in particular, exhibits the steepest and most stable M–S curve at 14 days, with high C^{-2} values across a wide potential range, signifying optimal passivation quality. However, when USS content exceeds 30%, as in US4FA1C and US5FA0C systems (Fig. 4f and g), passivation quality deteriorates. Although early-stage films (2–3 days) show improved electronic properties, the 14 days M–S curves exhibit a downward shift and decreased slope, indicating rising donor density and structural disorder. This is supported by the *C–V* results, which show renewed capacitance humps and increased temporal instability, suggesting enhanced ionic adsorption and film heterogeneity. Notably, in US5FA0C, the slope becomes significantly less steep at 14 days, implying that excessive USS introduces microstructural inhomogeneity or reaction product saturation, impeding film densification.

The widespread observation of two linear regions in the M–S plots, which deviates from the single slope of an ideal n-type semiconductor, points to the presence of multiple donor levels. As illustrated in the energy band model of Fig. 5, the dual-linear behavior is attributed to the ionization of two distinct donor species: the first linear region corresponds to shallow donors (*e.g.*, Fe^{2+} at tetrahedral sites), while the second reflects the contribution of deep donors (*e.g.*, Fe^{2+} at octahedral sites) activated at higher potentials.[27,58] The capacitance "humps" observed in *C–V* plots further corroborate the re-

Open Access Article. Published on 16 March 2026. Downloaded on 5/1/2026 12:22:37 AM.
This article is licensed under a Creative Commons Attribution-NonCommercial 3.0 Unported Licence.

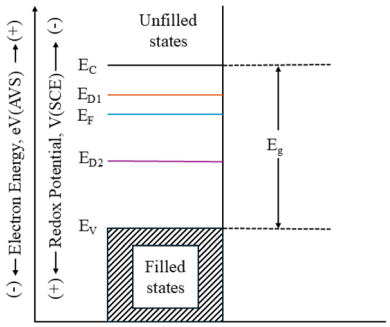

Fig. 5 Simplified energy level model of a n-type semiconductor in contact with an electrolyte solution under anodic polarization.

excitation of these defect states.[59] With increasing USS substitution, the *C–V* profiles evolve from pronounced hump features toward more stable responses, with optimal films (20–30% USS) showing minimal humps and stable capacitance, indicating dense and defect-resistant passive layers. In contrast, insufficient or excessive USS promotes defect activation, increasing heterogeneity and compromising long-term film stability.

To quantify the electronic properties of the n-type passive film, the donor densities were determined from M–S analysis. Assuming the Helmholtz-layer capacitance (CH) is much larger than the space-charge capacitance (CSC), the measured interfacial capacitance satisfies $C \approx$ CS, and the M–S relationship reduces to (eqn (1)):[58]

$$\frac{1}{C_{SC}{}^2} = \frac{2}{\varepsilon\varepsilon_0 N_D A^2} \times \left(E - E_{FB} - \frac{KT}{e}\right) \quad (1)$$

where ε is the dielectric constant of the passive film; ε_0 is the permittivity of free space; e is the elementary charge; K is Boltzmann's constant; T is absolute temperature; E is the applied potential (*vs.* SCE); and V_{fb} is the flat-band potential.

For films exhibiting two n-type donor populations, shallow donor density (N_{D1}) and deep donor density (N_{D2}) were extracted from the slopes S_1 (low-potential, "shallow" region) and S_2 (high-potential, "deep" region) of the linear segments:

$$N_{D1} = \frac{2}{\varepsilon\varepsilon_0 e S_1} \quad (2)$$

$$N_{D2} = \frac{2}{\varepsilon\varepsilon_0 e S_2} - N_{D2} \quad (3)$$

All SPS systems (Fig. 6a) exhibited a pronounced increase in N_{D1} from 2 h to 3 days, followed by more gradual changes through 14 days. Low-USS systems (US0FA5C, US1FA4C) showed the highest N_{D1} values at both 3 days and 14 days, indicating high concentrations of shallow donors that simultaneously suggest elevated point defect densities and potential film heterogeneity. Medium-USS systems (US2FA3C, US3FA2C) maintained moderate N_{D1} values with minimal temporal variation between 3 days and 14 days, implying stable shallow donor distributions and denser passive film structures. In contrast, high-USS systems (US4FA1C, US5FA0C) displayed the lowest early-stage N_{D1} values, with slight 14 days increases likely attributable to late-stage ion re-adsorption or partial film dissolution. As shown in Fig. 6b, N_{D2} remained negligible at 2 h for all systems, reflecting minimal deep donor ionization during initial passivation. From 3 days onward, N_{D2} increased markedly, peaking at 14 d. High-USS systems (US4FA1C, US5FA0C) exhibited the most pronounced N_{D2} growth, with final values exceeding 3×10^{20} cm^{-3}, indicating that excessive USS promotes deep donor formation *via* enhanced defect generation and ionic penetration. Medium-USS systems (US2FA3C, US3FA2C) maintained moderate N_{D2} levels at 14 d, demonstrating effective suppression of deep donor states and superior film compactness. Low-USS systems (US0FA5C, US1FA4C) showed limited N_{D2} growth, though their elevated N_{D1} suggests dominance of shallow defects over deep defect accumulation.

By combining the M–S-derived donor densities (N_{D1} and N_{D2}) with the *C–V* responses, an intermediate USS replacement (20–30%, *i.e.*, US2FA3C–US3FA2C) is identified as producing the most compact and electronically stable passive films. Passive films on steel in alkaline/concrete pore solutions typically exhibit n-type semiconducting behavior with two donor levels, and donor density is commonly used as an indicator of defect population and film protectiveness[27, 58]. The intermediate-USS mixes show moderate and time-stable N_{D1}, implying controlled shallow donors and reduced point-defect activity. More importantly, their N_{D2} at later ages is markedly lower than that of high-USS mixes, suggesting suppressed deep-donor

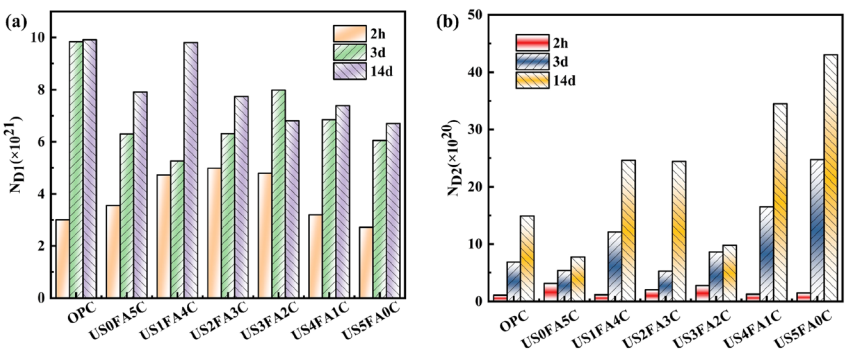

Fig. 6 (a) N_{D1} and (b) N_{D2} of reinforcing steel in different SPS systems.

© 2026 The Author(s). Published by the Royal Society of Chemistry

Open Access Article. Published on 16 March 2026. Downloaded on 5/1/2026 12:22:37 AM. This article is licensed under a Creative Commons Attribution-NonCommercial 3.0 Unported Licence.

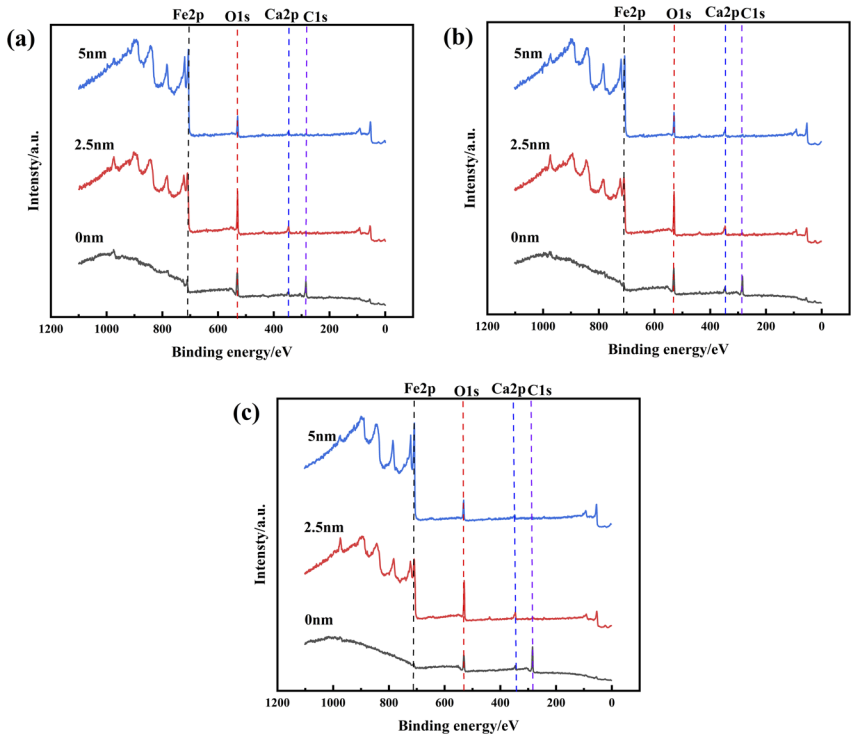

Fig. 7 Depth-profiling XPS reveals the through-thickness evolution of the passive film by tracking Fe 2p with sputtering depth (0–5 nm): (a) US5FA0C, (b) US3FA2C, and (c) US0FA5C.

development and a denser inner barrier. This is consistent with the *C–V* curves, which display only weak humps and near-overlapping profiles from 3 to 7 days, indicating a compact and homogeneous film with a stable interfacial charge response. These electronic features also agree with the EIS results, where intermediate-USS systems exhibit higher film resistance and more stable capacitive behavior over time.

3.3. Chemical composition of passivation film

3.3.1. Composition of passive film. To corroborate the electrochemical trends, the passive films were further characterized by XPS (including depth profiling), SEM/EDS, and AFM to resolve chemical states, elemental distribution, morphology, and surface roughness. The XPS survey spectra of passive films formed in US5FA0C, US3FA2C, and US0FA5C reveal predominant Fe and O signatures, with minor Ca and C contributions (Fig. 7). As sputtering depth increases (0 to 5 nm), Fe 2p and O 1s peak intensities progressively increase, whereas C 1s and Ca 2p signals steadily decline, indicating that carbon derives mainly from surface adsorbates and calcium primarily exists as $Ca(OH)_2/CaCO_3$ in the outermost layer. Among the systems, the high-USS blend (US5FA0C) exhibits significantly higher Fe 2p intensity at shallow depths, with persistently strong O 1s at greater depths, implying both high oxide content and structural porosity. The medium-USS system (US3FA2C) displays more stable Fe/O peak profiles and a rapidly diminishing Ca signal, consistent with a denser, homogeneous passive film. Conversely, the USS-free system (US0FA5C) shows the strongest surface Ca signal, denoting significant deposition. While its inner layer enriches in Fe oxides, these surface deposits likely compromise film compactness.

Fig. 8 presents the high-resolution XPS spectra of Fe 2p and O 1s for passive films formed on carbon steel surfaces after passivation in different solution systems. The Fe $2p_{3/2}$ spectrum can be deconvoluted into four characteristic peaks, while the O1s spectrum is associated with three characteristic peaks The specific parameters of these peaks are summarized in ref. 60–62. As shown in Fig. 8, the depth profiles exhibit the characteristic "bilayer" signature of passive films: the outer layer is dominated by Fe^{3+} oxides/hydroxides, transitioning. Inward to a Fe^{2+}-enriched dense barrier layer. Specifically, in the Fe $2p_{3/2}$ spectra, peaks associated with Fe^{3+} oxides/hydroxides (FeOOH, Fe_2O_3) and their satellite structures are most intense at the surface (0 nm) and progressively diminish from 2.5 nm to 5 nm, whereas Fe^{2+} peaks (FeO/Fe_3O_4) increase significantly with depth. Correspondingly, in the O 1s spectra, the lattice oxygen component O-1 increases with depth, while hydroxyl/defect oxygen O-2 and adsorbed water/carbonate O-3 decrease. This indicates that the outer layer is more hydroxylated and adsorption-rich, whereas the inner layer is more oxidized and structurally compact.

Among the mix proportions, US3FA2C exhibits the most favorable depth distribution: at 2.5–5 nm, it shows the highest proportions of Fe^{2+} and O-1 species, along with the lowest O-2/O-3 contents. This suggests a thicker, defect-scarce Fe^{2+}-enriched barrier layer, consistent with its stable M–S and *C–V* behavior. In contrast, both US0FA5C and US5FA0C display stronger signals from Fe^{3+}, –OH, and adsorbed species (O-2, O-3) at surface/near-surface regions. Although Fe^{2+} increases at

Open Access Article. Published on 16 March 2026. Downloaded on 5/1/2026 12:22:37 AM.
This article is licensed under a Creative Commons Attribution-NonCommercial 3.0 Unported Licence.

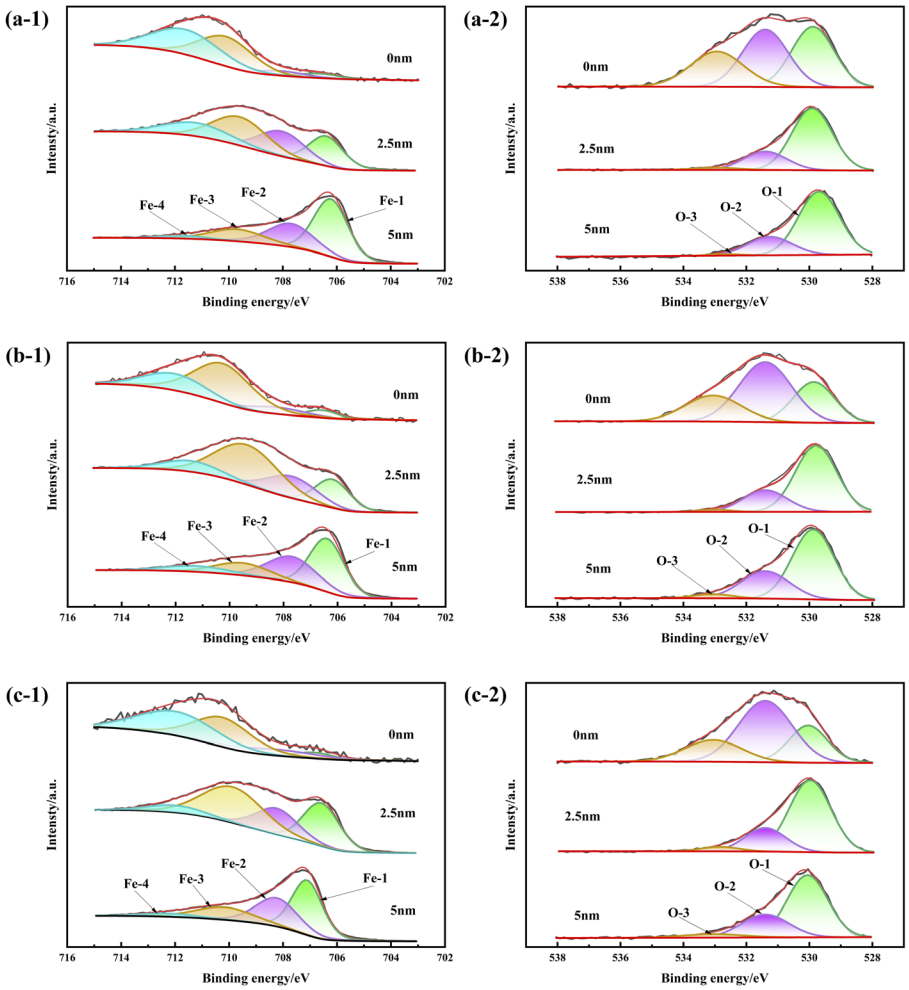

Fig. 8 High-resolution XPS spectra (Fe 2p and O 1s) identify the chemical states of passive films after 14 days passivation: (a) US5FA0C, (b) US3FA2C, and (c) US0FA5C.

5 nm, its proportion remains lower than in US3FA2C, indicating a looser outer layer with higher defect density, stronger ionic adsorption, and a relatively weaker inner barrier. These spectral trends align with electrochemical results, confirming that moderate USS content (US2FA3C, US3FA2C) favors dense, stable bilayer passive film formation, whereas excessively low or high USS content (US0FA5C, US5FA0C) promotes hydroxylation/adsorption and defect accumulation, compromising the film's electronic barrier capability.

Fig. 9 illustrates the compositional distribution and depth profile of iron species in passive films formed on carbon steel in US–FA–C solution. As shown in Fig. 9a, the Fe^{3+}/Fe^{2+} atomic ratio in US–FA–C is higher than in ultrafine steel slag-cement (US–C) systems but lower than in FA–C systems, indicating

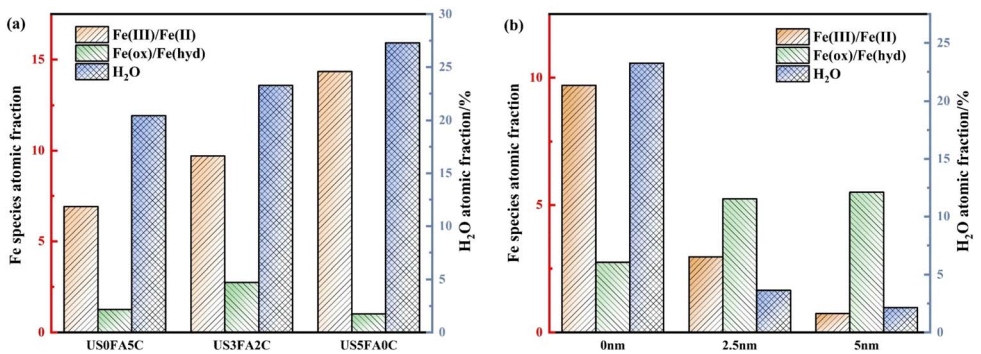

Fig. 9 XPS peak-fitting-derived atomic ratios quantify passive-film chemistry, including Fe oxidation-state and oxide/hydroxide-related fractions: (a) comparison among different SPS, and (b) variation with depth.

© 2026 The Author(s). Published by the Royal Society of Chemistry

Open Access Article. Published on 16 March 2026. Downloaded on 5/1/2026 12:22:37 AM.
This article is licensed under a Creative Commons Attribution-NonCommercial 3.0 Unported Licence.

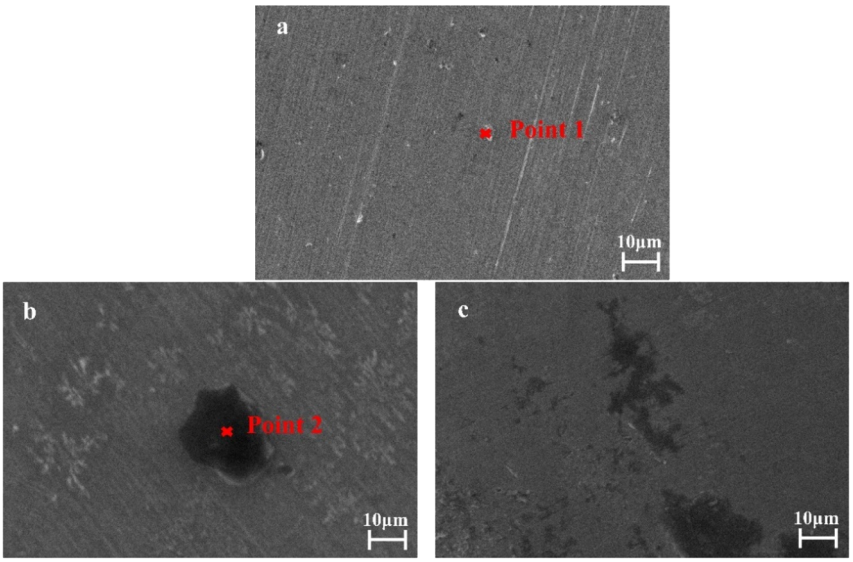

Fig. 10 SEM characterizes passive-film morphology and elemental distribution to evaluate surface integrity and local deposits: (a) US0FA5C, (b) US3FA2C, and (c) US5FA0C.

a moderate proportion of high-valence Fe^{3+} in its passive film. Concurrently, the oxides to hydroxides ratio ($Fe_{(ox)}/Fe_{(hyp)}$) peaks in US–FA–C, suggesting preferential formation of hydroxides. This structural feature correlates with enhanced oxidation and higher fractions of high-valence Fe species, likely due to synergistic USS–FA promotion of Fe^{2+} to Fe^{3+} oxidation. The moderate water content further implies optimal hydroxylation for structural stability without excessive hydration.

Fig. 9b reveals a significant decrease in the Fe^{3+}/Fe^{2+} ratio from the outer layer to the metal/film interface, accompanied by a corresponding increase in Fe^{2+} content. This trend reflects the typical bilayer structure: a high-valence (Fe^{3+}-rich) outer layer and a low-valence (Fe^{2+}-rich) inner layer. Concurrently, the $Fe_{(ox)}/Fe_{(hyp)}$ slightly increases toward the interface, indicating a gradual dominance of hydroxides. Combined with the rising Fe^{2+} content, this suggests enrichment of hydroxides near the interface. Water/hydroxyl content decreases inward, confirming that hydration and adsorption are confined to the outer layer. These depth profiles collectively demonstrate a beneficial bilayer protective structure in US–FA–C systems: a dense outer oxide and a coherent inner barrier tightly bonded to the substrate.

3.3.2. Thickness of passive film. Previous electrochemical analyses indicated comparable protective properties of passive films formed on carbon steel in SPS. However, these techniques lack compositional resolution. To address this gap, XPS analysis was conducted after 14 days immersion, corresponding to the stage where electrochemical tests showed negligible corrosion rates. Metallic Fe peaks appeared in all samples, confirming passive film thicknesses below 10 nm (the maximum photoelectron escape depth). And the film thickness exhibited compositional dependence in the sequence: US5FA0C (3.53 nm) > US3FA2C (3.40 nm) > US0FA5C (3.21 nm). Relative to US0FA5C, thickness increased by 5.9% for US3FA2C and 10.0% for US5FA0C, demonstrating distinct USS/FA regulatory effects on film growth. This thickening trend correlates directly with USS-induced pH elevation in the solution.

Table 5 EDS results of the corresponding areas in SEM images (wt%)

Region	C	O	Na	K	Ca	Mn	Fe
Zone 1	5.37	11.32	1.95	0.35	5.84	0.67	75.81
Zone 2	8.85	37.56	0.85	3.40	30.42	0.25	10.56

3.4. Top view morphology of the passive film

SEM and EDS results (Fig. 10 and Table 5) demonstrate the significant impact of USS content on passive film morphology and chemistry. In US0FA5C, the film shows a compact homogeneous surface with minimal defects; EDS point analysis reveals Fe-rich composition, indicating dominant dense iron oxides. With moderate USS (US3FA2C), localized pits emerge where defect regions exhibit Ca enrichment and O alongside reduced Fe, suggesting deposition of Ca-rich phases (*e.g.*, $CaCO_3$ or $Ca(OH)_2$) within defects. Excessive USS (US5FA0C) further degrades morphology, generating widespread porous deposits prone to initiating localized corrosion.

These findings indicate that while moderate USS balances alkalinity and passivation, excessive USS disrupts film uniformity, creating pathways for corrosive ions that compromise protective stability.

3.5. Three-dimensional morphology of the passivation film

Fig. 11 presents AFM surface topography of passive films formed on reinforcing steel after 14 days immersion in SPS with varying USS ratios. In US0FA5C (Fig. 11a), the film exhibits a uniform, wave-like morphology with finely distributed granular protrusions. Height variations range from −76.9 nm to 84.4 nm, and 3D images shows limited peak-valley fluctuations, indicating a compact, homogeneous structure. In US3FA2C (Fig. 11b), the surface roughness increases with irregular

Open Access Article. Published on 16 March 2026. Downloaded on 5/1/2026 12:22:37 AM.
This article is licensed under a Creative Commons Attribution-NonCommercial 3.0 Unported Licence.

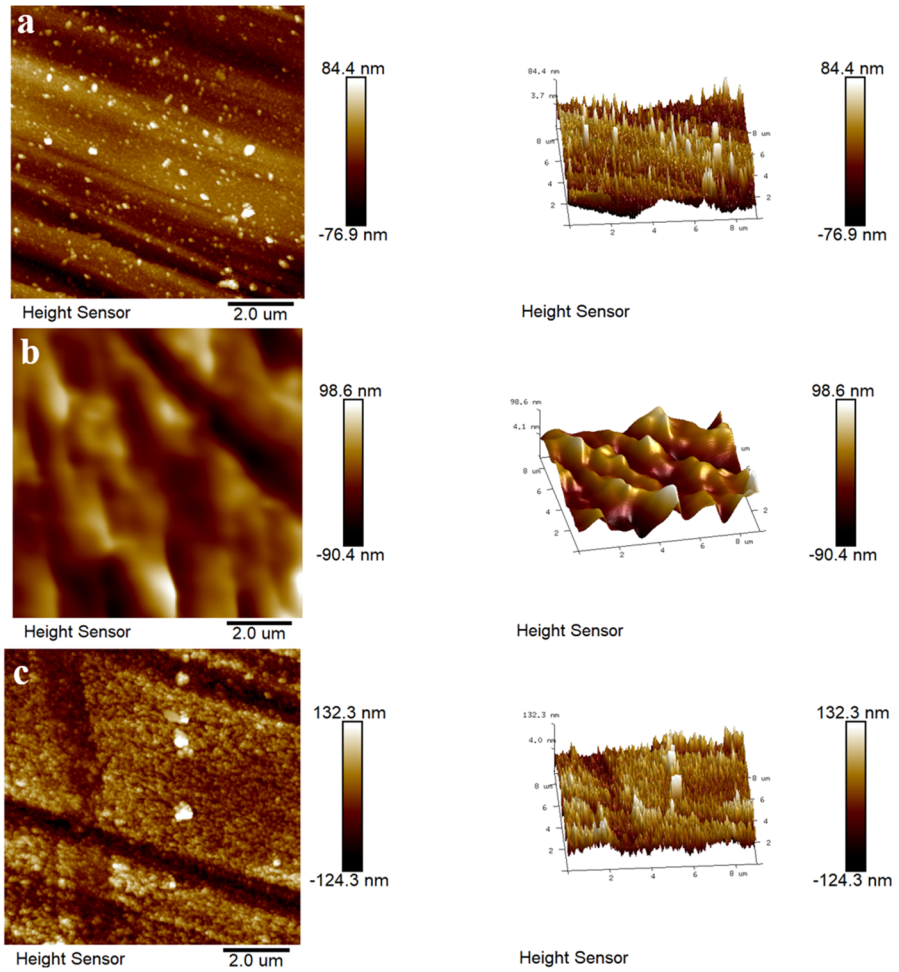

Fig. 11 AFM topography maps nanoscale surface morphology and height heterogeneity of passive films after 14 days passivation: (a) US0FA5C, (b) US3FA2C, and (c) US5FA0C.

protrusions/depressions The height range expands to −90.4 nm to 98.6 nm, and 3D images reveals pronounced local peaks, suggesting heterogeneous particle deposition and corrosion product accumulation. This results in slightly reduced uniformity *versus* US0FA5C. For US5FA0C (Fig. 11c), the film displays maximal roughness (−124.3 nm to 132.3 nm) with sharp protrusions and clustered peaks, denoting severe heterogeneity. This is attributed to excessive USS promoting localized deposition and nonuniform growth. Collectively, higher USS content increases surface roughness and degrades film uniformity, potentially compromising barrier properties. Fig. 12 presents the surface roughness of passive films formed on reinforcing steel in SPS for US0FA5C, US3FA2C, and US5FA0C. The results indicate pronounced roughness increases with rising USS content. The US0FA5C film exhibited the smoothest surface (R_q = 22.4 nm, R_a = 17.9 nm). In US3FA2C, R_q and R_a increased to 27.1 nm (a 20.9% increase) and 21.6 nm (a 20.6% increase) *versus* US0FA5C. The US5FA0C system showed the highest roughness (R_q = 36.4 nm, a 62.5% increase; R_a = 28.4 nm, a 58.6% increase), confirming a strong positive correlation between USS content and surface roughness. From a durability perspective, this roughness elevation expands the passive film's contact area with corrosive media, thereby facilitating Cl^- penetration and impairing long-term concrete durability. These results highlight the necessity of controlling USS dosage in concrete mixtures.

3.6. Effect of temperature

3.6.1. Charge transfer resistance of passive film. Fig. 13 shows the evolution of Nyquist plots for US3FA2C at 20 °C

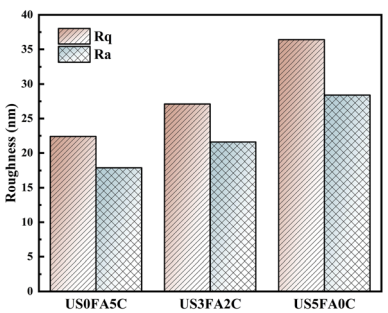

Fig. 12 AFM roughness parameters (R_a and R_q) quantify surface uniformity of passive films in different SPS.

© 2026 The Author(s). Published by the Royal Society of Chemistry

Open Access Article. Published on 16 March 2026. Downloaded on 5/1/2026 12:22:37 AM.
This article is licensed under a Creative Commons Attribution-NonCommercial 3.0 Unported Licence.

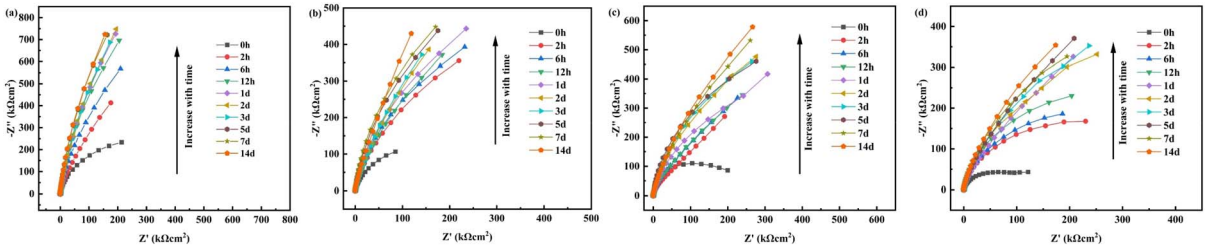

Fig. 13 Nyquist plots of US3FA2C passive film of the reinforcing steel passivated in different temperatures: (a) 20 °C, (b) 30 °C, (c) 40 °C and (d) 50 °C.

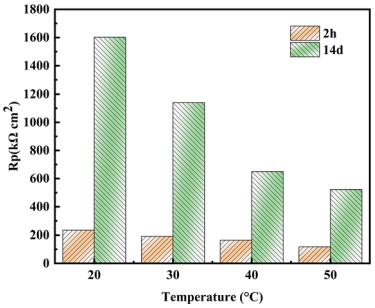

Fig. 14 R_p of reinforcing steel in different temperatures.

(room temperature), 30 °C, 40 °C, and 50 °C. All plots exhibit near-semicircular shapes with progressively expanding radii over immersion time, indicating continuous enhancement of film impedance and protectiveness. However, both the growth rate and stabilized impedance magnitude varied significantly with temperature. At 20 °C, impedance increased most significantly, achieving the largest semicircle radius after 14 d, denoting optimal film density and stability. At 30 °C, the evolution resembled 20 °C but with a marginally lower final value, implying minimal detrimental effects. At 40 °C, despite rapid initial growth, the final radius was substantially smaller than at lower temperatures, indicating that elevated temperature promotes defect generation/ion penetration, thereby reducing stability. At 50 °C, impedance growth was severely limited, with the 14 days radius reaching only 30–50% of the 20 °C value, confirming significant protection loss due to structural loosening, cracking, and pore formation. These results demonstrate that temperatures above 40 °C severely degrade long-term impedance, while 30 °C preserves film integrity.

Fig. 14 shows that for all temperatures, the R_p increases substantially from 2 h to 14 d, confirming that prolonged immersion enhances passive film protection in the US3FA2C system. At 20 °C, R_p rises from 233.6 kΩ cm^2 to 1602 kΩ cm^2 (an increase of 686%), accompanied by a slight decrease in the constant phase element exponent n from 0.93 to 0.92, indicating that the film remains highly capacitive and compact. At 30 °C, a similar trend is observed, but the final R_p (1140 kΩ cm^2) is lower than at 20 °C, suggesting moderate thermal degradation of the film. At 40 °C, the R_p growth markedly slows, reaching only 650 kΩ cm^2 at 14 d, indicating that higher temperatures significantly compromise film integrity. The most severe deterioration is seen at 50 °C, where R_p increases only from 118 kΩ cm^2 to 523 kΩ cm^2, and n decreases to 0.88, reflecting increased surface heterogeneity and porosity. The Y_0 values generally increase with time and temperature, consistent with enhanced ionic conductivity and reduced barrier properties at elevated temperatures. Collectively, the results indicate that while passivation deteriorates over time at all temperatures, temperatures above 30 °C begin to reduce film resistance, with degradation becoming pronounced at 40 °C and especially severe compromise at 50 °C.

3.6.2. Electronic performance of passive film. At 20 °C (Fig. 15a), the C^{-2} of the passive film increases significantly with immersion time, with the overall curve shifting downward and the slope gradually decreasing. This indicates that over time, both the space-charge layer capacitance decreases and the depletion layer width increases, which, in the context of passive film growth, reflects a gradual increase in film thickness; furthermore, the decreasing slope suggests a marked increase in defect concentration (acceptor density). As immersion time

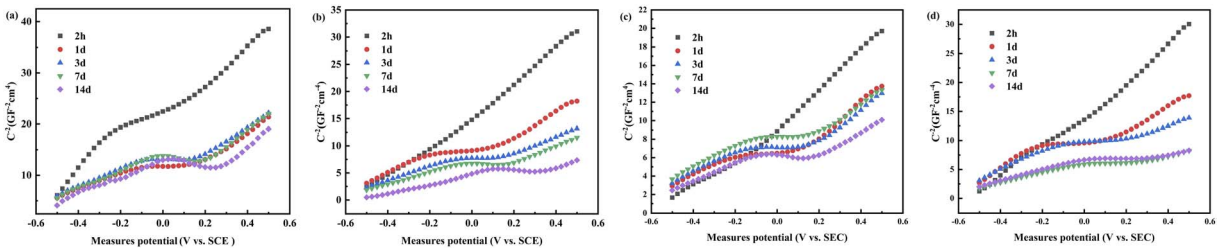

Fig. 15 M–S plots of US3FA2C passive film of the reinforcing steel passivated in different temperatures: (a) 20 °C, (b) 30 °C, (c) 40 °C and (d) 50 °C.

Open Access Article. Published on 16 March 2026. Downloaded on 5/1/2026 12:22:37 AM.
This article is licensed under a Creative Commons Attribution-NonCommercial 3.0 Unported Licence.

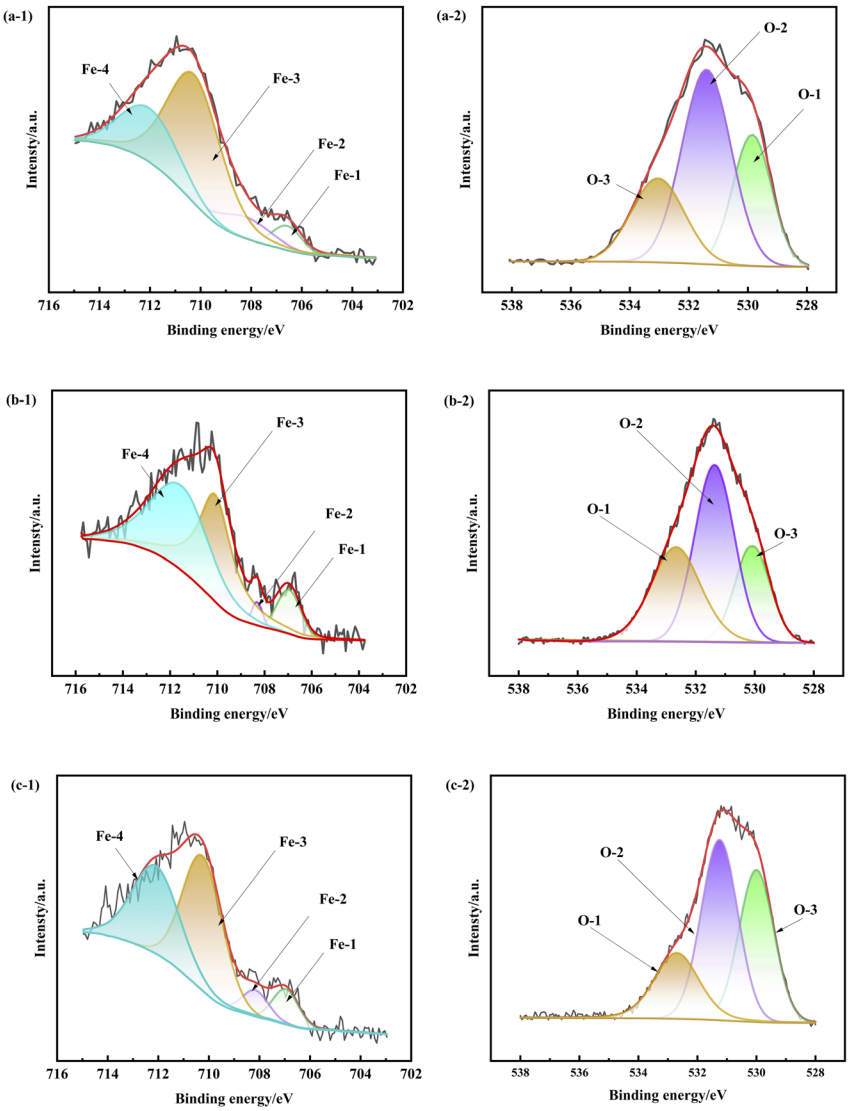

Fig. 16 High-resolution XPS tracks temperature-dependent changes in Fe 2p and O 1s chemical states of the passive film in US3FA2C: (a) 30 °C, (b) 40 °C, and (c) 50 °C.

proceeds, the rates of change of these parameters slow down and tend to stabilize. This implies that at ambient temperature, the passive film can continue to grow, with its structure becoming progressively denser, and its electrical properties approaching stability, thereby enhancing its protective performance.

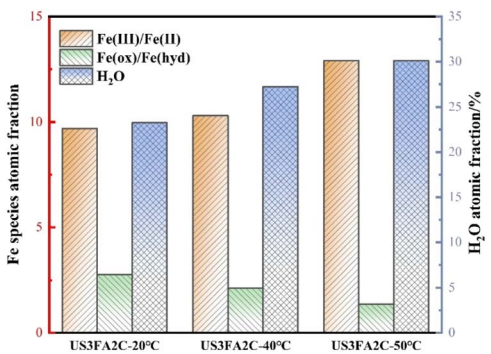

Fig. 17 Atomic ratios of iron species in the passive film on steel immersed in US3FA2C solution at different temperatures.

At 30 °C (Fig. 15b), although the C^{-2} curve shows a similar downward trend to 20 °C, its values are consistently lower. This suggests slightly higher carrier concentration and reduced structural compactness compared to 20 °C. At 40 °C (Fig. 15c), defect concentrations exceed those at lower temperatures with limited curve shifting, indicating suppressed defect repair and film densification. At 50 °C (Fig. 15d), defect concentration peaks among tested temperatures and the downward trend weakens significantly, demonstrating that elevated temperature promotes defect generation/accumulation, severely degrading film stability and protectiveness. Collectively, rising temperature accelerates initial film formation but exacerbates defect accumulation and compromises long-term protection, with degradation apparent above 40 °C and most severe at 50 °C.

3.6.3. Composition of passive film. Fig. 16 displays the high-resolution Fe 2p and O 1s XPS spectra of passive films

© 2026 The Author(s). Published by the Royal Society of Chemistry

Open Access Article. Published on 16 March 2026. Downloaded on 5/1/2026 12:22:37 AM.
This article is licensed under a Creative Commons Attribution-NonCommercial 3.0 Unported Licence.

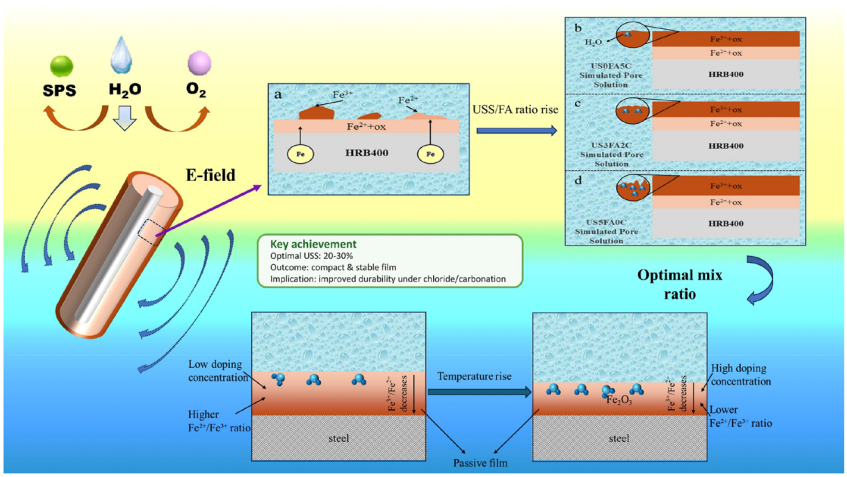

Fig. 18 Proposed mechanism and key outcomes linking USS/FA ratio to pore-solution chemistry and passive-film evolution on steel (optimal USS: 20–30%).

formed on reinforcing steel in US3FA2C solutions at various temperatures. Compared to 20 °C, the relative intensity of Fe^{3+} species increases at 40 °C and further rises at 50 °C, while Fe^{2+} contributions diminish. This indicates enhanced oxidation alongside elevated defect generation tendencies at higher temperatures. Concurrently, the O-1 fraction slightly decreases with rising temperature, whereas O-2 and O-3 fractions increase, revealing enhanced hydroxylation and adsorbed surface species. These trends reflect higher defect density and passive film hydration at 40–50 °C, correlating with reduced structural compactness and compromised long-term protective capacity.

At 20 °C, the passive film exhibits an optimal Fe^{3+}/Fe^{2+} ratio and higher $Fe_{(ox)}/Fe_{(hyd)}$ ratio, indicating an ordered crystal structure with reduced ionic transport pathways. This yields R_p nearly 47% higher than films formed at 40 °C, confirming superior passivation. Notably at 50 °C (Fig. 17), the $Fe_{(ox)}/Fe_{(hyd)}$ ratio drops to 1.36. This compositional shift combines with increased defect density and elevated chemisorbed water (H_2O component increasing by 32% in O 1s) to synergistically degrade film integrity. The mechanism involves intrinsic hygroscopicity of FeOOH, which promotes capillary-driven water enrichment at defects, forming nanoscale percolating hydration pathways. These structural heterogeneities substantially lower the diffusion barrier for Cl^-.9

3.7. Literature comparison and scheme summary

To position the present findings relative to representative reports, a comparison is summarized in Table S1. A comparison with representative literature on steel passivation in simulated pore solutions and blended-binder systems is provided in Table S1, highlighting that the present work uniquely links USS-driven ionic redistribution to passive-film electronic defect descriptors (N_{D1}/N_{D2} and C–V) and cross-validates them with EIS to identify an optimal USS replacement window (20–30%). The proposed mechanism and key achievements, including the optimal USS window (20–30%), are summarized in Fig. 18.

4. Conclusions

This study investigates the synergistic effects of USS and FA along with varying temperature on the passivation kinetics and stability of passive films on reinforcing steel in USS – FA -OPC ternary systems. The pore solution chemistry, electrochemical properties, semiconductor behavior, film composition and morphology were systematically analyzed. Based on experimental findings and preceding discussions, the following conclusions are drawn:

(1) The incorporation of 50% FA significantly enriches K+ in the pore solution but reduces pH to 12.56, below the passivation threshold. A 30% USS content optimally counteracts this effect by dissolving Ca-bearing phases, restoring pH to 12.95, and re-establishing an alkalinity level conducive to stable passivation.

(2) Passivation kinetics and film stability are highly sensitive to the USS/FA ratio, with the 30% USS blend exhibiting the most favorable performance. This formulation achieves rapid potential stabilization and the highest charge-transfer resistance over 14 days, indicating a dense and durable passive layer. In contrast, high-FA systems passivate slowly due to inadequate alkalinity, while high-USS systems form heterogeneous films with compromised long-term stability.

(3) The semiconductor properties of the passive film are governed by USS content. The optimal USS–FA blend minimizes both N_{D1} and N_{D2} donor densities, leading to a compact and defect-resistant film. Deviations from this optimum significantly increase defect densities, particularly N_{D2} in high-USS systems, aggravating deep-layer disorder and ionic permeability.

(4) A moderate USS content promotes the formation of a superior bilayer structure, characterized by a Fe^{3+}-rich outer layer and a Fe^{2+}-enriched inner barrier. This configuration, rich in lattice oxygen and low in hydroxyl/water content within the 2.5–5 nm region of the passive film, ensures high density and excellent barrier properties. Excessive FA encourages defective Ca-rich deposits, while high USS increases porosity and ionic ingress.

Open Access Article. Published on 16 March 2026. Downloaded on 5/1/2026 12:22:37 AM. This article is licensed under a Creative Commons Attribution-NonCommercial 3.0 Unported Licence.

(5) USS dosage critically influences film morphology and roughness. While low USS yields a smooth, compact film, and moderate USS slightly increases roughness (nearly 21%) while maintaining integrity, excessive USS (50%) raises roughness by over 60%, resulting in porous, heterogeneous films with elevated susceptibility to chloride penetration.

(6) Temperature exerts a critical influence on film stability. Optimal passivation occurs at ≤30 °C, whereas temperatures ≥40 °C promote defect formation, increase hydration, reduce Fe^{2+} content, and elevate adsorbed water, collectively leading to a more permeable and less protective film.

These findings provide a mechanistic basis for optimizing waste-incorporated low-carbon cementitious systems, bridging the gap between solid waste valorization and composition-driven durability design in sustainable construction. Future perspectives and challenges. The proposed optimal USS window and the associated electronic indicators should be validated in mortar/concrete specimens under realistic chloride ingress and carbonation, where transport and microcracking may alter passivation kinetics. The coupled effects of temperature and oxygen availability also warrant long-term evaluation, because pore solution chemistry and film structure evolve with hydration and aging. In addition, interactions with aggressive or competitive ions (*e.g.*, Cl^- and SO_4^{2-}) should be systematically assessed to clarify their roles in deep-donor activation and inner-barrier stability.

Author contributions

Ying Lin & Zhiwei Wu: investigation, methodology, data curation, formal analysis, writing – original draft. Zhengxian Yang: conceptualization, investigation, supervision, project administration, funding acquisition, writing – review & editing. Hesong Jin: validation, writing – review & editing.

Conflicts of interest

The authors declare that they have no known competing financial interests or personal relationships that could have appeared to influence the work reported in this paper.

Data availability

The data supporting this article are available from the corresponding author.

Supplementary information (SI): table S1: comparison of this work with representative literature on steel passivation in simulated pore solutions and blended-binder systems. See DOI: https://doi.org/10.1039/d5ra09738j.

Acknowledgements

This research was supported by the National Natural Science Foundation of China (52478241) and Fujian Provincial Science and Technology Plan (2024I0006).

Notes and references

1 K. Li, Z. Yang, D. Nicolaides, M. Liang, B. Briseghella, G. C. Marano and Y. Zhang, *Constr. Build. Mater.*, 2024, **438**, 137219.
2 X. Xiong, Z. Yang, X. Yan, Y. Zhang, S. Dong, K. Li, B. Briseghella and G. C. Marano, *Constr. Build. Mater.*, 2023, **398**, 132512.
3 K. Li, Z. Yang, S. Dong, P. Ning, D. Ye and Y. Zhang, *Constr. Build. Mater.*, 2025, **471**, 140712.
4 J. Sun, S. Hou, Y. Guo, X. Cao and D. Zhang, *Buildings*, 2024, **14**, 614.
5 Z. Yang, X. Xiong, K. Li, B. Briseghella, G. C. Marano and S. Chen, *Cem. Concr. Compos.*, 2024, **145**, 105352.
6 Q. Li, J. Li, S. Zhang, X. Huang, X. Wang, Y. Wang and W. Ni, *Energies*, 2023, **16**, 2376.
7 Z. Yang, X. Xiong, S. Chen, B. Briseghella, G. C. Marano and Y. Zhang, *J. Build. Eng.*, 2023, **72**, 106682.
8 Z. Tariq and A. Bahadori-Jahromi, *Eng. Sustain.*, 2025, 1–30.
9 Z. Geng, N. Yao, X. Zhou and J. Shi, *Cem. Concr. Compos.*, 2023, **143**, 105236.
10 M. H. Shehata, M. D. Thomas and R. F. Bleszynski, *Cem. Concr. Res.*, 1999, **29**, 1915–1920.
11 W. Deng, R. Xiong, X. Zhai, K. Huang, L. Li, Y. Zong, H. Wang, J. Zhai, H. Lai and N. Mao, *Environ. Sci. Pollut. Res.*, 2024, **31**, 55917–55934.
12 Q. Wang, J. Yang and P. Yan, *Powder Technol.*, 2013, **245**, 35–39.
13 X. Han, J. Feng, Y. Shao and R. Hong, *Powder Technol.*, 2020, **370**, 176–183.
14 S. Joiret, M. Keddam, X. R. Nóvoa, M. Pérez, C. Rangel and H. Takenouti, *Cem. Concr. Compos.*, 2002, **24**, 7–15.
15 M. Sánchez, J. Gregori, M. Alonso, J. García-Jareño and F. Vicente, *Electrochim. Acta*, 2006, **52**, 47–53.
16 P. Ghods, O. B. Isgor, J. Brown, F. Bensebaa and D. Kingston, *Appl. Surf. Sci.*, 2011, **257**, 4669–4677.
17 M. Sánchez-Moreno, H. Takenouti, J. García-Jareño, F. Vicente and C. Alonso, *Electrochim. Acta*, 2009, **54**, 7222–7226.
18 Y. Li and Y. F. Cheng, *Appl. Surf. Sci.*, 2017, **396**, 144–153.
19 G. S. Parkinson, *Surf. Sci. Rep.*, 2016, **71**, 272–365.
20 L. Xu, P. Wu, X. Zhu, G. Zhao, X. Ren, Q. Wei and L. Xie, *Corros. Sci.*, 2022, **207**, 110563.
21 M. S. Senn, J. P. Wright and J. P. Attfield, *Nature*, 2012, **481**, 173–176.
22 B. Zhang, J. Wang, B. Wu, X. Guo, Y. Wang, D. Chen, Y. Zhang, K. Du, E. Oguzie and X. Ma, *Nat. Commun.*, 2018, **9**, 2559.
23 X.-X. Yu, J. Han, J. R. Scully and L. D. Marks, *Acta Mater.*, 2021, **213**, 116898.
24 H. Parangusan, J. Bhadra and N. Al-Thani, *Emerg. Mater*, 2021, **4**, 1187–1203.
25 Z. Jin, X. Zhao, Y. Du, S. Yang, D. Wang, T. Zhao and Y. Bai, *Constr. Build. Mater.*, 2022, **319**, 126142.
26 H. Long, L. Chen, B. Dong, Y. Sun, Y. Yan and C. Chen, *Constr. Build. Mater.*, 2022, **360**, 129567.

© 2026 The Author(s). Published by the Royal Society of Chemistry

Open Access Article. Published on 16 March 2026. Downloaded on 5/1/2026 12:22:37 AM. This article is licensed under a Creative Commons Attribution-NonCommercial 3.0 Unported Licence.

27 J. Williamson and O. B. Isgor, *Corros. Sci.*, 2016, **106**, 82–95.
28 K. Natkunarajah, K. Masilamani, S. Maheswaran, B. Lothenbach, D. Amarasinghe and D. Attygalle, *Cem. Concr. Res.*, 2022, **156**, 106780.
29 A. Vollpracht, B. Lothenbach, R. Snellings and J. Haufe, *Mater. Struct.*, 2016, **49**, 3341–3367.
30 R. Chen, J. Hu, Y. Ma, W. Guo, H. Huang, J. Wei, S. Yin and Q. Yu, *Corros. Sci.*, 2020, **165**, 108393.
31 M. S. Badar, K. Kupwade-Patil, S. A. Bernal, J. L. Provis and E. N. Allouche, *Constr. Build. Mater.*, 2014, **61**, 79–89.
32 S. Diamond, *Cem. Concr. Res.*, 1981, **11**, 383–394.
33 Z. Yang, M. Zheng, X. Xiong, Y. Zhang, B. Briseghella and G. C. Marano, *J. Build. Eng.*, 2024, **97**, 111002.
34 T. Teratoko, N. Maruoka, H. Shibata and S.-y. Kitamura, *High Temp. Mater. Processes*, 2012, **31**, 329–338.
35 S. Duan, H. Wu, K. Zhang, H. Liao, Z. Ma and F. Cheng, *J. Build. Eng.*, 2022, **62**, 105368.
36 X. Wu, H. Zhu, X. Hou and H. Li, *Cem. Concr. Res.*, 1999, **29**, 1103–1106.
37 N. S. Labra, *Películas pasivas formadas en presencia de iones silicato y ortofosfato para mitigar la corrosión del acero de contrucción en presencia de iones nitrito*, Universidad Nacional de Mar del Plata, 2024.
38 C. Li, A. Wang, L. Xie, X. Deng, K. Liao, J.-a. Yang, T. Li and F. Hao, *J. Mater. Chem. A*, 2019, **7**, 24150–24163.
39 S. S. Shinde, N. K. Wagh, S. H. Kim and J. H. Lee, *Adv. Sci.*, 2023, **10**, 2304235.
40 A. Matamoros-Veloza, R. Barker, S. Vargas and A. Neville, *ACS Appl. Mater. Interfaces*, 2020, **12**, 49237–49244.
41 R. Hamai, Y. Shirosaki and T. Miyazaki, *J. Biomed. Mater. Res., Part B*, 2017, **105**, 1924–1929.
42 M. M. Seckler, *Cristalização industrial a partir de soluções: sobre fundamentos e aplicações*, Universidade de São Paulo, 2011.
43 Z. Du, R. Shi, Z. Mi, Z. Xu, Y. Zhu, S. Liu, K. Gao, A. A. Volinsky and X. Pang, *Corros. Sci.*, 2025, **247**, 112776.
44 W. Piasecki, K. Szymanek and R. Charmas, *Adsorption*, 2019, **25**, 613–619.
45 H. I. Adegoke, F. A. Adekola, O. S. Fatoki and B. J. Ximba, *Pol. J. Environ. Stud.*, 2013, **22**, 7–24.
46 D. Landolt, *Corrosion and Surface Chemistry of Metals*, EPFL press, New York, 2007.
47 A. L. Harmat, M. Morga, J. L. Lutkenhaus, P. Batys and M. Sammalkorpi, *Appl. Surf. Sci.*, 2023, **615**, 156331.
48 L. Wang, A. Seyeux and P. Marcus, *J. Electrochem. Soc.*, 2020, **167**, 101511.
49 S.-I. Pyun and J.-W. Lee, *Progress in Corrosion Science and Engineering II*, Springer, New York, 2012.
50 K. Neuhaus, P. Mowe and M. Winter, *RSC Appl. Interfaces*, 2025, **2**, 620–633.
51 Y. Dou, Z. Li, J. Cheng and Y. Zhang, *Materials*, 2020, **13**, 5214.
52 L. S. Wan, M. Hirata, T. Oyamoto, T. Kanda and K. H. Tan, *Case. Stud. Constr. Mat.*, 2025, **22**, e04364.
53 R. W. Revie and H. H. Uhlig, *An Introduction to Corrosion Science and Engineering*, John Wiley & Sons Inc, New Jersery, 2008.
54 Y. Li, S. Zhu, J. Xian, X. Li, Y. Zhao and S. Wang, *Sci. Rep.*, 2022, **12**, 11822.
55 A. Schackow, C. Effting, I. R. Gomes, I. Z. Patruni, F. Vicenzi and C. Kramel, *Appl. Therm. Eng.*, 2016, **103**, 1362–1369.
56 X. Feng, T. Wu, J.-l. Luo and X. Lu, *Cem. Concr. Compos.*, 2020, **112**, 103651.
57 S. Manso Blanco and A. Aguado de Cea, *Mater.Construcc.*, 2017, **67**, 1–10.
58 J. Williamson and O. Isgor, *Adv. Civ. Eng. Mater.*, 2016, **5**, 80–106.
59 Y. Kocak and S. Nas, *Constr. Build. Mater.*, 2014, **73**, 25–32.
60 M. C. Biesinger, B. P. Payne, A. P. Grosvenor, L. W. Lau, A. R. Gerson and R. S. C. Smart, *Appl. Surf. Sci.*, 2011, **257**, 2717–2730.
61 Y. Lin, Z. Yang and J. Xu, *Appl. Surf. Sci.*, 2025, **720**, 165347.
62 Y. Lin, F. Sun and Z. Yang, *Constr. Build. Mater.*, 2025, **499**, 144073.

© 2026 The Author(s). Published by the Royal Society of Chemistry